Journal of Materials Chemistry A

Accepted Manuscript

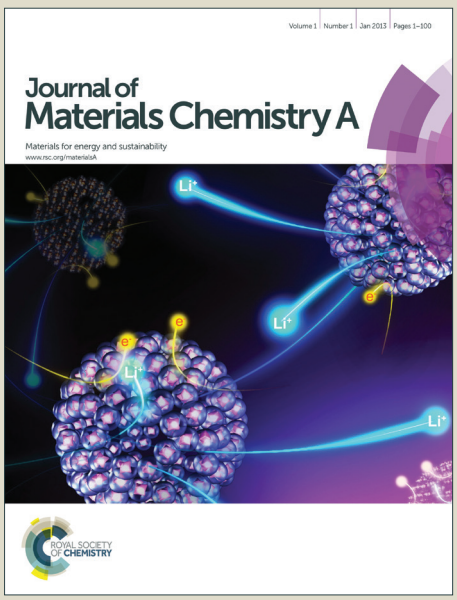

ROYAL SOCIETY OF CHEMISTRY

www.rsc.org/materialsA

Journal Name

RSCPublishing

ARTICLE

In Situ Nano-Coating on $Li_{1.2}Mn_{0.52}Ni_{0.13}Co_{0.13}O_2$ with Layered@Spinel@Coating Layer Heterostructure for Lithium-Ion Batteries

Cite this: DOI: 10.1039/xoxxoooooox

Received ooth xoxxoooooox,
Accepted ooth xoxxoooooox

DOI: 10.1039/xoxxoooooox

www.rsc.org/

Bing Li[a], Chao Li[b], Jijun Cai[b], Jinbao Zhao[a,b*]

The lithium-rich manganese-based layered oxides with composition of $xLi_2MnO_3 \cdot (1-x)LiMO_2$ (M = Mn, Co, Ni, etc) are attractive, due to their high discharge capacity. However, the concerns over Li_2MnO_3-$LiMO_2$ composite cathodes such as high irreversible capacity and poor rate performance remain to be the main obstacle to commercialization. Here we introduce a thin chromium oxide layer and a spinel metal oxide layer to doubly coat on the surface of $Li_{1.2}Mn_{0.52}Ni_{0.13}Co_{0.13}O_2$ (LMNCO) by the spray drying process as well as an inducer of Layered@Spinel@Coating Layer heterostructure to achieve better electrochemical performance. X-ray diffraction (XRD), scanning electron microscope (SEM), and high-resolution transmission electron microscope (HR-TEM) results confirm the successful formation of a chromium oxide layer on the surface of LMNCO without destroying its intrinsic structure. The reduced irreversible capacity loss and improved cycling stability are ascribed to the coating layer and the heterostructure. Furthermore, fast voltage fading of the solid solutions of layered transition metal oxides is also alleviated.

Introduction

Rechargeable lithium-ion batteries (LIBs) are one of the most promising energy storage devices for electric vehicles (EV) and hybrid electric vehicles (HEV), because of their high energy density, high power density, stable charge/discharge cycling and long calendar life [1]. The most commercially used cathode material in high energy LIBs is layered $LiCoO_2$, which is expensive due to the use of rare-earth metal Cobalt (Co). The olivine $LiFePO_4$ and spinel $LiMn_2O_4$ have been regarded as the alternatives to $LiCoO_2$. However, their volume and weight energy densities are low in the practical application. Recently, many research groups pay attention to lithium-rich manganese-based layered oxides with composition of $xLi_2MnO_3 \cdot (1-x)LiMO_2$ (M = Mn, Co, Ni, etc), due to their high discharge capacity, low cost and good safety [2-5]. But the challenges of Li_2MnO_3-$LiMO_2$ composite cathodes such as high irreversible capacity [6] and poor rate performance [7] remain to be the main obstacles to commercialization.

Surface modification has been regard as a promising strategy to enhance the electrochemical performance of Li-rich layered oxide materials. Coating materials, such as PI [8], PPY [9], V_2O_5 [10],ZrO_2 [11],CeO_2 [12],Li_3VO_4 [13], had been applied to stabilize the surface structure, avoid side reactions between cathode materials and electrolyte under high voltage and suppress HF corrosion to materials. As a result, the cycle performance and cycle stability of Lithium-rich layered oxide materials is improved [14-16]. Among these coatings, the AlF_3 coating layer can induce the transformation of the layer phase to a spinel phase [17]. The formation of a spinel phase can play an important role as a fast lithium ion conductor and help to improve the rate capacity, because the cubic-close-packing in layered and spinel lithium-metal oxide cathodes permit the structural compatibility [17-19].

Hence, to improve the electrochemical properties of layered lithium-rich metal oxide, a composite (Layered@Spinel@ Coating Layer) with core-shell structure, in which double layers consisting of Li-Cr-O and spinel lithium-metal oxide respectively are coated on the layered cathode material, is designed and in-situ synthesized by nano-coating technology. In the heterostructure composite, the merits of the integrated "layered and spinel" structure is combined through a facile process. Good electrochemical performances can be predicted from the comprehensive design route. Firstly, the coating layer could separate the host particles from the electrolyte to reduce the surficial side reaction as well as alleviate the dissolution of Mn ion, benefiting the cycle stability. Secondly, the harmonious coexistence of layered and spinel phase on nano-scale size can accelerate lithium ion transportation through independently choosing the fastest and shortest transportation path, ensuring the outstanding rate capability.

Experimental section

Material preparation

The material of $Li_{1.2}Mn_{0.52}Ni_{0.13}Co_{0.13}O_2$ (LMNCO) was synthesized by a facile carbonate co-precipitation method in our previous paper [20]. In detail, the stoichiometric amounts of $MnSO_4 \cdot H_2O$ (≥99.0%, AR, Sinopharm Chemical Reagent Co.

Ltd), $CoSO_4•7H_2O$ (≥99.5%, AR, Sinopharm Chemical Reagent Co. Ltd), $NiSO_4•6H_2O$ (≥99.5%, AR, Sinopharm Chemical Reagent Co. Ltd) were mixed in 150 ml de-ionized water. Then, 50 ml ethanol (AR, Sinopharm Chemical Reagent Co. Ltd) was added into this solution. The concentration of metal ions in this mixed solution was 0.015 mol·L^{-1}. After stirring for 2 h, 200 ml NH_4HCO_3 (AR, Sinopharm Chemical Reagent Co. Ltd) solution (0.045 mol·L^{-1}) was added quickly to prepare carbonate compounds. The obtained carbonate compounds with mixed metal cation were dried and then heated at 500 ºC for 5 h to obtain the solid solutions of transition metal oxides with spherical morphology. After that, the metal oxides were mechanically mixed well with $LiOH•H_2O$ (≥95.0%, AR, Sinopharm Chemical Reagent Co. Ltd). Then the mixture was sintered at 480 ºC for 4 h in air, and further calcined at 800 ºC for 12 h to obtain the uncoated cathode material $Li[Li_{0.2}Mn_{0.52}Ni_{0.13}Co_{0.13}]O_2$ (U-LMNCO). The heating rates were all maintained at 5 ºC·min^{-1}.

Preparation of coating $Li_{1.2}Mn_{0.54}Ni_{0.13}Co_{0.13}O_2$ (T-LMNCO) samples: certain amounts of $Cr(NO_3)_3 \cdot 9H_2O$ (≥99.0%, AR, Sinopharm Chemical Reagent Co. Ltd) and $NH_3 \cdot H_2O$ (GR, Sinopharm Chemical Reagent Co. Ltd) were dissolved in 200 ml deionized water. The PH of this mixed solution was controlled 7 ~ 8 by the ammonia. Then, 0.5 g $Li_{1.2}Mn_{0.52}Ni_{0.13}Co_{0.13}O_2$ powder was added. After ultrasonic treatment and stirring for 1 h, the obtained suspension was directly fed into a benchtop Buchi mini-spray dryer (B-290, Buchi, Switzerland) and spray-dried at 130 °C, with aspirator 100%. Then, the obtained power was calcined at 500 ºC in a tube furnace for 5 h in air and then cooled to room temperature to get T-LMNCO. In this way, the 1 wt%, 2 wt% and 4 wt% T-LMNCO, meaning the weight ratios are 1 %, 2 % and 4 % respectively. The sample U-LMNCO was prepared as follows: 0.5 g $Li_{1.2}Mn_{0.52}Ni_{0.13}Co_{0.13}O_2$ powder was dispersed into 200 ml deionized water. After ultrasonic treatment and stirring for 1 h, the solution was directly fed into a benchtop Buchi mini-spray dryer (B-290, Buchi, Switzerland) and spray-dried at 130 °C, with aspirator 100%. Then, the obtained power was calcined at 500 ºC in a tube furnace for 5 h in air and then cooled to room temperature.

Material characterization

Crystal characterization of the materials was performed with a Rigaku Ultima IV (Rigaku Corporation) using Kα radiation operated at 40 kV and 30 mA. Data were collected over the range of 10°≤ 2θ ≤90° and analysized using PDXL-2 analysis software (Rigaku Corporation). Scanning electron microscope (SEM) was performed on S-4800 (Hitachi Corporation). Elemental mappings of the prepared samples were carried out with an energy dispersive X-ray detector (EDX). Transmission electron microscope (TEM) was carried out on JEM-2100 (JEOL). The elementary composition of the materials were determined by inductive coupled plasma-atomic emission spectroscopy (ICP-AES), carried out on plasma 1000 (NCS Testing Technology, China). X-ray photoelectron spectra (XPS) of these samples were recorded on Quantum 2000 (Physical electronics). Raman spectrums were obtained on Xplora (Horiba Corporation).

Electrochemical measurements

Electrochemical performances of these materials were evaluated in CR2016-type coin-cell. The electrolyte was 1 mol·L^{-1} $LiPF_6$(Battery Grade, Shenzhen Capchem Co.Ltd) salt dissolved in a mixed solution of ethylene carbonate (EC) (Battery Grade, Shenzhen Capchem Co.Ltd) and dimethyl carbonate (DMC) (Battery Grade, Shenzhen Capchem Co.Ltd) with a volume ratio of 1 : 1 The active materials, acetylene black, and polyvinylidene fluoride (PVDF) (Battery Grade, Songbai Chemical Industry Co.Ltd) were mixed in a weight ratio of 80:10:10 in N-methyl-2-pyrrolidene (NMP) (Battery Grade, Songbai Chemical Industry Co.Ltd) to form a slurry. The slurry was coated onto battery aluminum foil and dried at 80 ºC to obtain an electrode sheet. The coin cells were assembled by sandwiching a separator celgard 2400 (Celgard Co.Ltd) between the electrode and Li metal foil (China Energy Lithium Co. Ltd)in an Ar-filled glove box (Mbraun, Germany). The mass loading for all the cells was controlled at about 3.6 mg. The charge and discharge tests were performed galvanostatically between 2.0 and 4.8 V using a Landian CT2001A (Wuhan, China) battery testing system at room temperature at different current rates with current densities from 25 mA·g^{-1} (0.1 C) to 500 mA·g^{-1} (2 C). All the capacity were calculated based on weight of the active material in the electrode. The initial charge-discharge test was studied at 0.1 C and the cycling test was measured at 1 C after the first cycle at 0.1 C. The voltage fading means a voltage change at the point of capacity discharge to 50% per cycle. The data of voltage fading can be directly collected by a Landian CT2001A (Wuhan, China) battery testing system. The cyclic voltammograms of the first three cycles was tested on an electrochemical workstation (CHI660E) at a scanning rate of 0.1 mV·s^{-1}. The electrochemical impedance spectroscopy (EIS) of the cells was conducted on an electrochemical workstation (Autolab PGSTA T302 N) with an amplitude voltage of 10 mV and frequency range of 0.01 Hz-10 kHz.

Results and discussion

The compositions of three materials of T-LMNCO are experimentally determined by ICP and are shown in Table 1. The elemental ratios of Mn/Ni/Co are in excellent agreement with the targeted stoichiometries. The content of chromium also agrees with the theoretical value. Owing to the much faster evaporation of water through spray drying process, the content of lithium remains unchanged.

Table 1 Compositions U-LMNCO and 1%, 2%, 4% T-LMNCO Electrode Materials

	Li /mole	Mn /mole	Co /mole	Ni /mole	Cr /mole
U-LMNCO	1.20	0.52	0.13	0.13	0
1%T-LMNCO	1.20	0.52	0.13	0.13	0.011
2%T-LMNCO	1.20	0.52	0.13	0.13	0.021
4%T-LMNCO	1.20	0.52	0.13	0.13	0.044

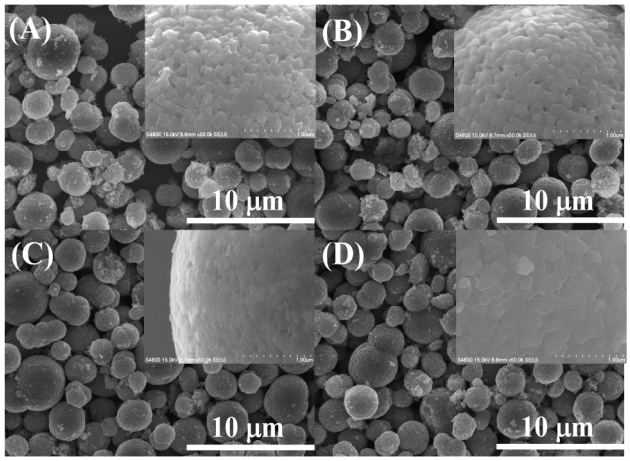

Fig. 1 SEM images of U-LMNCO (A); 1 wt% T-LMNCO (B); 2 wt% T-LMNCO (C); 4 wt% T-LMNCO (D)

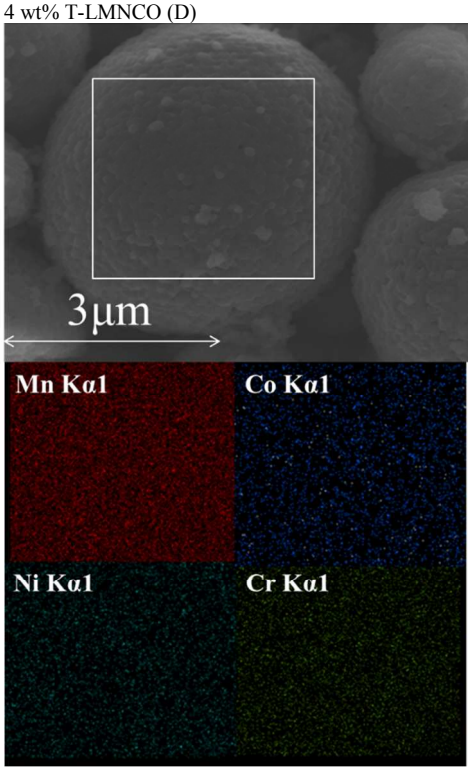

Fig. 2 EDS dot-mapping for elements of 2 wt% T-LMNCO

The SEM images of T-LMNCO and U-LMNCO are shown in Fig. 1A-D. All these secondary particles are spherical in a size ranging from 4 μm to 6 μm, composed of primary particles with a size of 100 nm. For the T-LMNCO sample (B-D in Fig. 1), the differences of the particles can also be seen clearly due to the low quantity of coating layer. Compared to the rough surface of the U-LMNCO, the surface of T-LMNCO became much smoother with the mass of coating layer increased. In the present work, EDS was selected to check the coating layer on the surface of 2 wt% T-LMNCO (Fig. 2). The measured results of EDS showed that all the elements including Cr were distributed homogeneously on the surface of the particles. A thinner coating layer could be observed from the TEM images (shown in Fig. 3), which be designed to reduce the contact between bulk material and electrolyte.

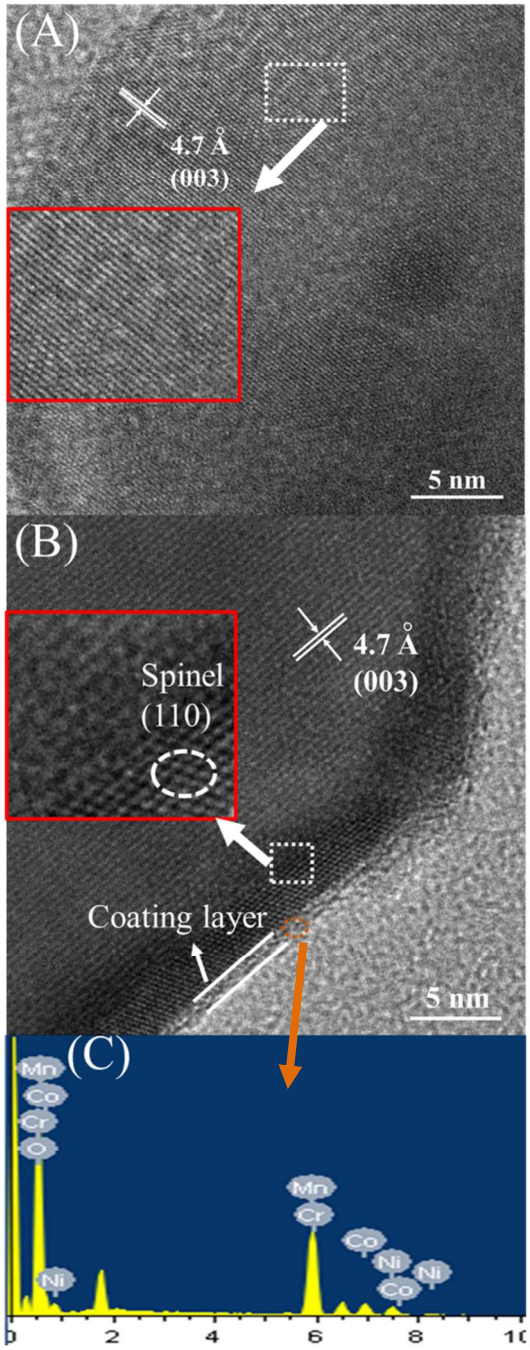

Fig. 3 High magnification TEM images of U-LMNCO (A), the insert is an enlarged TEM image in the white square area ; 2 wt% T-LMNCO (B) , the insert is an enlarged TEM image in the white square area; The corresponding surface EDS spectrum of 2 wt% T-LMNCO (C) in the orange oval area in (B).

The formation of integrated layered-spinel structures was evidenced explicitly by comparative TEM analysis T-LMNCO and U-LMNCO (Fig. 3). These inter-planar spacing observed

both in T-LMNCO and U-LMNCO were all about 4.7 Å (Fig. 3), which is in accordance with the d-spacing of (003) crystal planes of the layer structure. It means that the coating layer doesn't alter the basic structure of LMNCO. However, Figure 3B showed the electron diffraction pattern of T-LMNCO sample indexed to the (110) zone of the cubic spinel structure (corresponding to the red square region). As for LMNCO, no spinel phase was observed in its TEM image (Fig.3A). Selected area EDS elemental analysis (the orange oval area region in Fig.3B) shown in Fig.3C confirmed the existence of Chromium element in the coating layer. Therefore, the comparative images provided clear evidence to verify the presence of integrated layered@spinel structure in T-LMNCO sample. As the previous reports [21], when introducing coating layer onto the surface of cathode material, the second calcination process even at low temperature could give rise to the rearrangement of metal ions and to form other interesting and unexpected phase transition, which could be beneficial or harmful to the electrochemical performances. In the T-LMNCO sample, it is speculated that the layer-to-spinel phase transformation was triggered by chromium oxide coating during the calcination process, with extra lithium ions chemically leaching from internal Li-rich cathode, which is similar as others reported[17]. For the Li-rich layered structure $(Li)_{3a}[LixM1-x]_{3b}O_2$, the transition metal ions locate in 3b octahedron sites, lithium ions occupy the 3a tetrahedron sites and a small portion of lithium ions locate in 3b octahedron sites in the transition metal layer [22]. During the metal ions rearrangement process, part of the transition metal ions migrate from the 3b into the 16d octahedron sites and the lithium ions move into the 8a tetrahedron sites, forming the cubic spinel structure $(Li)_{8a}[M_2]_{16}dO_4$(Fig. S2) [23].

Fig. 4 shows the XRD patterns of T-LMNCO and U-LMNCO powder. The diffraction peaks of all samples are the same and can be indexed as a hexagonal α-$NaFeO_2$ structure (space group: 166, R-3m), with a few broad peaks between 2θ = 20 ° and 25 ° (Fig. 4A). There are several features in these XRD results. Firstly, the diffraction peaks among 20 °-25 ° (2θ) , caused by the superlattice ordering of Li and Mn in the transition metal layers in the Li-rich layered oxides, confirm the existence of Li_2MnO_3 [2]. Secondly, the formation of ordered lamellar structures in the hexagonal structure can be indicated by the (018)/(110) peaks splitting [24]. In these samples, the (018)/(110) doublets are well separated, indicating the formation of highly ordered lamellar structures. Lastly, the important feature is the ratio of the intensities of (003)/(104) peaks. A well-ordered sample should have a much bigger value than 1.2, while a heavily ion-mixed sample should have a value much smaller than 1.2 [25]. The ratios for these four materials are 1.55 (U-LMNCO), 1.52 (1 wt% T-LMNCO), 1.42 (2 wt% T-LMNCO) and 1.11(5 wt% T-LMNCO), respectively. The value decreased with the weight of chromium oxide increasing, and the value of 10 wt% T-LMNCO sample is only 0.96 (Fig. S1 supporting information). It is likely that the migration of parts of Li^+ from the transition metal layer to the coating layer during material synthesis might increase this ratios via the creation of spinel-like phase [17]. This inference is proved by the Raman spectral analysis (Fig. 5), and it will be discussed in the next part. However, as for the T-LMNCO samples, the spinel-related peaks corresponding to $LiMn_2O_4$ or $Li_{1-x}Mn_2O_4$ ($Fd\bar{3}m$) had been marked (Fig. 4). The shoulder peaks assigned to the $Fd\bar{3}m$ spinel phase have been pointed out by the red star (LMO) or purple star ($L_{1-x}MO$). All the data could confirm the existence of the $Fd\bar{3}m$ spinel phase in the T-LMNCO sample, reported in the previous papers[19, 26-28]. These peaks became more evident with the increase of coating amount, especially for 10 wt% T-LMNCO sample (Fig.S1 supporting information). The XRD data present that the nano-coating protective layer on the particle surface induced a structure transformation from layer to the spinel partially in the host material.

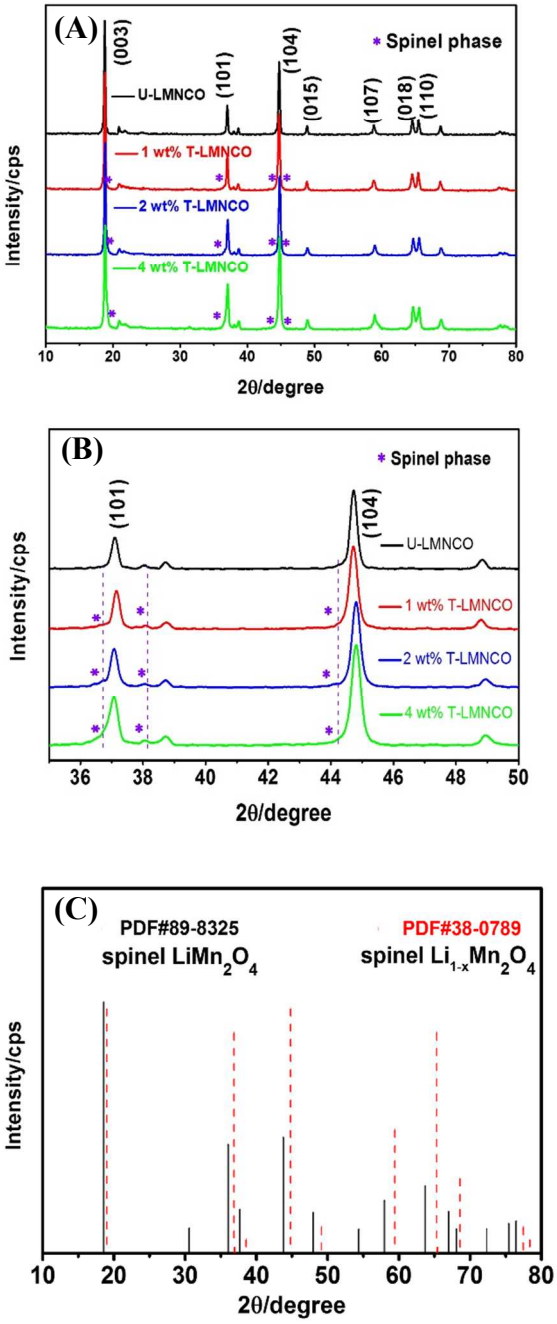

Fig. 4 XRD patterns of 1 wt%, 2 wt%, 4 wt% T-LMNCO and U-LMNCO (A); Enlarged view of XRD patterns for 1 wt%, 2 wt%, 4 wt% T-LMNCO and U-LMNCO samples within a specific 2θ range (B); Bragg positions for typical spinel $LiMn_2O_4$ and $Li_{1-x}Mn_2O_4$ ($Fd\bar{3}m$) (C).

It has been indicated by the Raman spectral analysis in the next section. As shown in Fig. 5, the Raman band at 422 cm^{-1} associated with the Li_2MnO_3 component which is seen in the

spectra of the U-LMNCO sample. The other two significant Raman peaks which appear at around 473 and 600 cm^{-1} in the spectrum of the U-LMNCO sample belong to the bending E_g and stretching A_{1g} modes, respectively [29], are blue shifted to higher values in the T-LMNCO samples, 484 and 624 cm^{-1}(2 wt% T-LMNCO sample), and a broad peak around 500 cm^{-1} and 624 cm^{-1}. These shifts in Raman spectrums indicate the structure changes after the chromium oxide nano-coating, and could be ascribed to a spinel-type cation disordering (a characteristic band at 625 cm^{-1}). It is assumed that, in the T-LMNCO sample, the layer-to–spinel phase transformation was triggered by chromium oxide nano-coating during the calcination process, with extra lithium ions chemically leached from the Li-rich cathode. When the lithium amount decreased, the spinel component will be formed on the outermost layer. Meanwhile, the degree of disorder metal vibration increased as the spinel component arising, resulting in the peak of Raman spectrums broadened and the unsmooth curves.

Possible oxidation states of transition metal ions in the layered composite material were checked using XPS, and the corresponding spectra in the narrow binding energy range for Mn, Co, Ni, and Cr are presented in Fig. 6. Binding energies observed for the elements were in good agreement with the values reported for similar oxide cathode materials [30]. The major peaks at binding energies of ca. 642, 780, and 855 eV are attributed to Mn^{4+}, Co^{3+} and Ni^{2+}, respectively. Cr 2p peaks are distinct in the spectra for the 2 wt% coated sample (Fig. 6).The binding energy obtained here is 586.0 eV for Cr $2p_{1/2}$, showing the valence state of Cr is Cr (III).

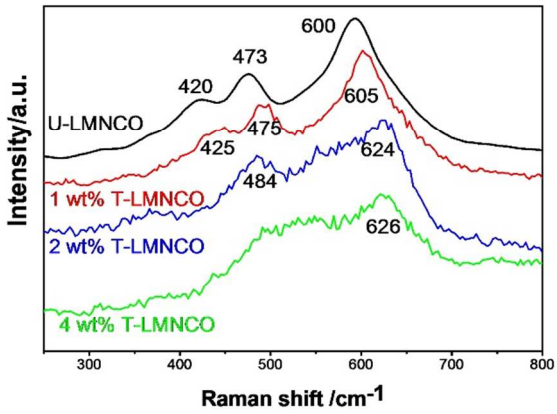

Fig. 5 Raman spectrums of U-LMNCO, 1 wt%, 2 wt% T-LMNCO and 4 wt% T-LMNCO.

The first charge/discharge curves cycled between 2--4.8 V at 0.1 C and the cyclic voltammetry curves of prepared LMNCO/Li cell are compared in Fig. 7 and Fig. 8. During the charging process, all the cells exhibited two distinguishable stages, a smoothly sloping voltage profile below 4.5 V corresponding to Li^+ deintercalation from the $LiMn_{1/3}Co_{1/3}Ni_{1/3}O_2$ component, and a long plateau around 4.5 V, corresponding to the extraction of lithium ion from Li_2MnO_3 structure and structural rearrangement, respectively [31]. Obviously, the voltage plateau of T-LMNCO below 4.5 V is longer than that of the U-LMNCO, due to the reduced layered structure. And then, a 2.8 V oxidation/reduction peak (Fig. 8) appeared in all the T-LMNCO samples and gradually increased in intensity with increasing chromium oxide coating amount expect the U-LMNCO sample, which is the characteristic peak of spinel phase, indicating the structure transformation induced by the nano-coating and in agreement with the previous XRD and Raman analysis. It is proposed that one of the Li^+ cations removed during the activation of Li-rich layered component are intercalated into the spinel component (vacant 16c octahedral sites) below 3.0 V[32]. The oxidation peak of spinel phase was observed from the subsequent charging cycles at 2.9 V indicating the good reversibility of spinel redox. Furthermore, the corresponding dQ/dV curves (Fig. S4) clearly show a reduction peak around 2.8 V, which is related to the Li^+ intercalation mechanism of the newly formed spinel phase component, implying that the spinel phase also participates in the electrochemical reaction in the first charge/discharge process.

As shown in the Fig. S2, the reduction peak of the 4 wt%-LMNCO sample between 3--4 V shift to 3 V at the first discharging process, then back to 3.7 V in the following cycles, while this obvious phenomenon does not occurred in the other samples. Furthermore, this is the reason why the first charge-discharge curves of 4 wt%-LMNCO sample (Fig. 7) is a little different from the remaining three. An electrochemical activation may be occurred during the first cycle, since the thicker chromium oxide coating layer.

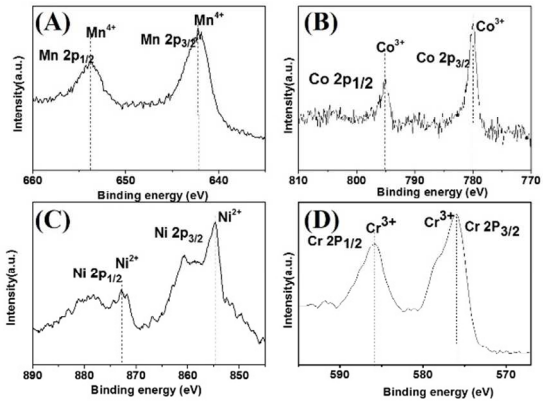

Fig. 6 X-ray photoelectron (A) Mn 2p, (B) Co 2p, (C) Ni 2p and (D) Cr 2p spectra of 2 wt% T-LMNCO

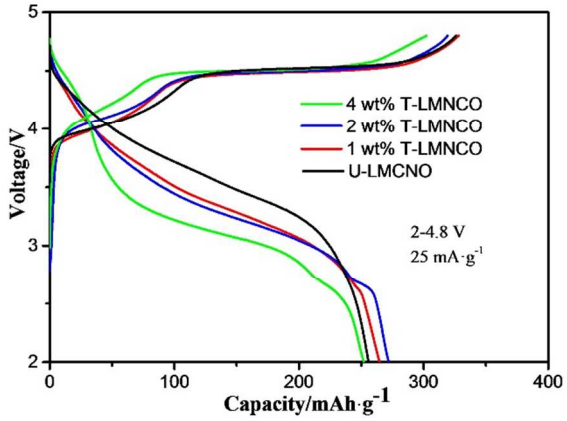

Fig. 7 First charge-discharge curves of all four samples

As expected, this ~2.8 V peak cannot be observed in U-LMNCO. In addition, reversible redox peaks at about 4.7 V are

observed only in the T-LMNCO samples (Fig. 8& Fig. S4), which may be attributed to the $Ni^{2+/4+}$ in the induced spinel phase of high-voltage material $LiNi_xMn_{2-x}O_4$. It could be concluded that although the coating layer cannot stop the voltage drop [33], it may delay the voltage drop, owing to a high potential oxidation-reduction peak.

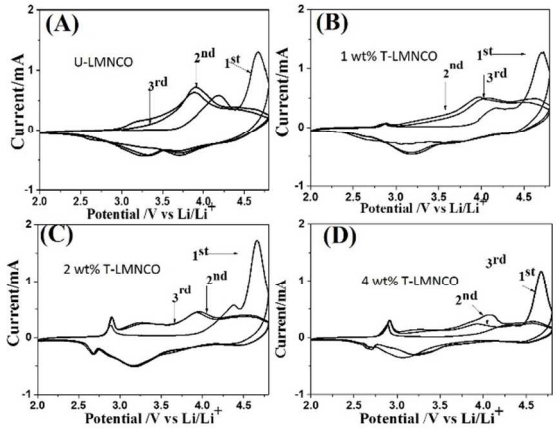

Fig. 8 Cyclic voltammograms of the first three cycles (A) U-LMNCO, (B) 1 wt% T-LMNCO, (C) 2 wt% T-LMNCO and (D) 4 wt% T-LMNCO

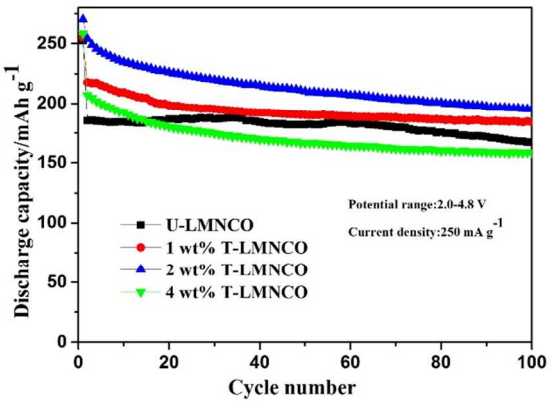

Fig. 9 Cycling performances of the cells with the synthesized cathode materials at 1 C rate

The cycle performances of the T-LMNCO and U- LMNCO samples were evaluated at 1 C (250 $mA \cdot g^{-1}$) between 2.0 and 4.8 V after an initial 0.1 C activation cycle. As shown in Fig. 9, all the T- LMNCO samples deliver higher discharge capacity than the U-LMNCO sample. After 100 cycles, the 2 wt% T-LMNCO sample exhibits a discharge of 195.2 $mAh \cdot g^{-1}$, whereas the U-LMNCO and 4 wt% T-LMNCO samples decay to 166.9 and 158.5 $mAh \cdot g^{-1}$. It should be noted that, for the T-LMNCO, the spinel interlayer has stable 3D framework and achieves better structural compatibility with the layered cores, which can increase the structural stability and restrain further structural transformation [34]. Furthermore, the outmost coating layer could also stabilize the surface structure of electrode, reduce side reactions between the electrolyte and electrode surface, protect the active materials from HF attack and avoid the metal ions dissolution, especially Mn metal ion (Table.S1). It will be hoped that, if the Li^+ could insert into the coating layer from the bulk material forming a stable structure, whenever it happened during the preparation process or the electrochemical cycling, the rich-Li layered@spinel@coating layer composite structure may be prepared.

The cycle performances of synthesized LMNCO/Li cell at 0.5 C and 1 C rate are displayed in Fig. 10. Obviously, the issue of voltage fading still existed in the three samples. Serious voltage fading with cycling was observed in U-LMNCO sample, owing to the continuous undesired layered-to-spinel phase transformation. However, the voltage fading rate of T-LMNCO samples effectively slowed down, especially the 2 wt% T-LMNCO sample, as shown in Fig. 10. The intergrated layered-spinel phase of T-LMNCO sample is more beneficial for reducing the speed of voltage fading.

In order to systematically evaluate the rate properties of the U-LMNCO and T-LMNCO samples, electrochemical cycles under high charge/discharge rates were tested in this work. As shown in Fig.11, the 2 wt% T-LMNCO sample has the best rate performance among all samples, especially at the 2000 $mA \cdot g^{-1}$. For the heterostructure, the "spinel phase" has 3D Li^+ diffusion channels that can greatly enhance the transmission rate of Li^+ and facilitate Li^+ intercalation/deintercalation processes. The data of EIS measurements also agree with this result (Fig. S5). It is easy to find that the values of both R_f and R_{ct} decrease after surface modification, which reveals that the coating layer could suppress interaction between the cathode surface and the electrolyte. However, excessive "spinel phase" appeared with the amount of chromium oxide increased, the main structure of the material may be ruined together with layered structure collapse, resulting in a bad rate performance. Therefore, the superior rate performance of the T-LMNCO sample can be reasonably attributed to both the stable integrated layered-spinel structures and the positive affection of the nano-coating.

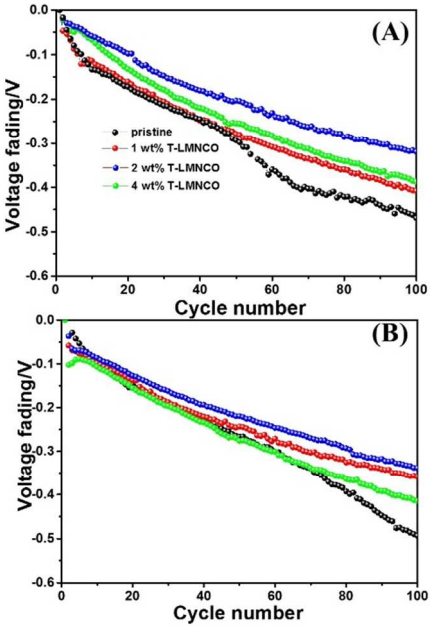

Fig. 10 Comparison of voltage fading rates of the cells with the synthesized cathode materials during cycling at 0.5 C and 1 C rate.

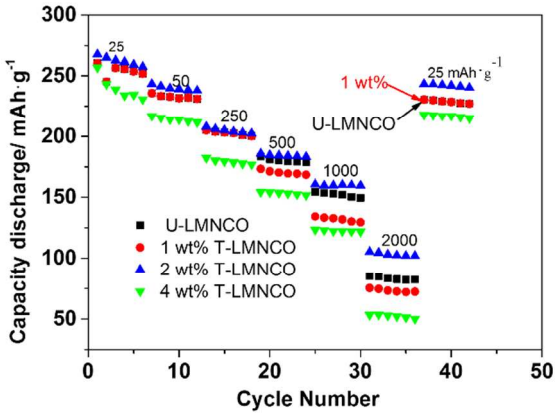

Fig. 11 The rate performances of the cells with different cathode materials

Conclusions

In conclusion, we combined phase transformation and nano-coating technology to successfully synthesize Li-rich cathode composite with improved cycleability for Li-ion batteries. In the composite, a spinel phase were in situ formed along the layered bulk/coating interface with the assistance of Li^+ migration from the bulk to the coating layer. In addition, the coating layer acting as a fast electron conduction path, effectively suppressed side reactions between cathode and electrolyte and stabilized the surface structure of electrode. The good electrochemical performances, including the improved cycling stability, the reduced first irreversible capacity loss, and the discharge capacity, as well as the low voltage fading rate, demonstrated the positive roles of integrated layered@spinel structures and nano-coating. It is anticipated that the current experimental findings may provide some technical insights to further improve the capacity of lithium ion positive materials, paving the way for the next-generation high performance lithium-ion batteries.

Acknowledgements

The authors gratefully acknowledge the financial supports from the National High Technology Research and Development Program of China (863 Program, No.2013AA050901), Key Project of Science and Technology of Fujian Province (No.2013H6022), and Science and Technology Bureau of Xiamen (Grant No. 3502Z20133004).

Notes and references

[a] State Key Lab of Physical Chemistry of Solid Surfaces, Department of Chemistry, Collaborative Innovation Center of Chemistry for Energy Materials, College of Chemistry and Chemical Engineering, Xiamen University, Xiamen, 361005, P. R. China.
[b] School of Energy Research, College of Energy, Xiamen University, Xiamen, 361005,P.R. China.
E-mail: jbzhao@xmu.edu.cn

† Electronic Supplementary Information (ESI) available:

XRD patterns of 10 wt% T-LMNCO; Scheme of layered-to-spinel structural transformation; dQ/dV curves of all the samples for three cycles at 0.1 C rate; Comparison of voltage fading rates of the cells with the synthesized cathode materials during cycling at 0.5 C and 1 C rate; EIS spectrum of U-LMNCO and 2% T-LMNCO; The amount of metal dissolved into the electrolyte

1. B. Dunn, H. Kamath and J. M. Tarascon, *Science*, 2011, **334**, 928-935.
2. M. M. Thackeray, S.-H. Kang, C. S. Johnson, J. T. Vaughey, R. Benedek and S. A. Hackney, *Journal of Materials Chemistry*, 2007, **17**, 3112-3125.
3. S. K. Martha, J. Nanda, G. M. Veith and N. J. Dudney, *Journal of Power Sources*, 2012, **199**, 220-226.
4. Christopher S. Johnson, Naichao Li, Christina Lefief, John T. Vaughey and M. M. Thackeray, *Journal of Materials Chemistry*, 2008, **20**, 6095-6106.
5. G.-Y. Kim, S.-B. Yi, Y. J. Park and H.-G. Kim, *Mater. Res. Bull.*, 2008, **43**, 3543-3552.
6. J. M. Zheng, P. H. Xu, M. Gu, J. Xiao, N. D. Browning, P. F. Yan, C. M. Wang and J. G. Zhang, *Chemistry of Materials*, 2015, **27**, 1381-1390.
7. J. Zheng, M. Gu, A. Genc, J. Xiao, P. Xu, X. Chen, Z. Zhu, W. Zhao, L. Pullan, C. Wang and J. G. Zhang, *Nano letters*, 2014, **14**, 2628-2635.
8. J. Zhang, Q. Lu, J. Fang, J. Wang, J. Yang and Y. NuLi, *ACS Appl Mater Interfaces*, 2014, **6**, 17965-17973.
9. C. Wu, X. Fang, X. Guo, Y. Mao, J. Ma, C. Zhao, Z. Wang and L. Chen, *Journal of Power Sources*, 2013, **231**, 44-49.
10. J. Wang, S. Yao, W. Lin, B. Wu, X. He, J. Li and J. Zhao, *Journal of Power Sources*, 2015, **280**, 114-124.
11. Z. Wang, E. Liu, L. Guo, C. Shi, C. He, J. Li and N. Zhao, *Surface and Coatings Technology*, 2013, **235**, 570-576.
12. W. Yuan, H. Z. Zhang, Q. Liu, G. R. Li and X. P. Gao, *Electrochimica Acta*, 2014, **135**, 199-207.
13. Q. Fu, F. Du, X. Bian, Y. Wang, X. Yan, Y. Zhang, K. Zhu, G. Chen, C. Wang and Y. Wei, *J Mater Chem A*, 2014, **2**, 7555-7562.
14. S. T. Myung, K. Amine and Y. K. Sun, *Journal of Materials Chemistry*, 2010, **20**, 7074-7095.
15. J. H. Wang, Y. Wang, Y. Z. Guo, Z. Y. Ren and C. W. Liu, *J Mater Chem A*, 2013, **1**, 4879-4884.
16. H. Zhuo, S. Wan, C. He, Q. Zhang, C. Li, D. Gui, C. Zhu, H. Niu and J. Liu, *Journal of Power Sources*, 2014, **247**, 721-728.
17. Y. K. Sun, M. J. Lee, C. S. Yoon, J. Hassoun, K. Amine and B. Scrosati, *Adv Mater*, 2012, **24**, 1192-1196.
18. X. Feng, Z. Yang, D. Tang, Q. Kong, L. Gu, Z. Wang and L. Chen, *Physical chemistry chemical physics : PCCP*, 2015, **17**, 1257-1264.
19. Y. Chen, K. Xie, C. Zheng, Z. Ma and Z. Chen, *ACS Appl Mater Interfaces*, 2014, **6**, 16888-16894.
20. B. Li, Y. Yu and J. Zhao, *Journal of Power Sources*, 2015, **275**, 64-72.
21. F. Wu, N. Li, Y. F. Su, H. F. Shou, L. Y. Bao, W. Yang, L. J. Zhang, R. An and S. Chen, *Adv Mater*, 2013, **25**, 3722-3726.
22. Z. Xu, J. Wang, K. Zhang, H. Zheng, Z. X. Dai, J. Gui and X. Q. Yang, *ACS Appl Mater Interfaces*, 2014, **6**, 1219-1227.
23. D. Mohanty, A. S. Sefat, S. Kalnaus, J. L. Li, R. A. Meisner, E. A. Payzant, D. P. Abraham, D. L. Wood and C. Daniel, *J Mater Chem A*, 2013, **1**, 6249-6261.
24. T. Ohzuku, A. Ueda, M. Nagayama, Y. Iwakoshi and H. Komori, *Electrochimica Acta*, 1993, **38**, 1159-1167.
25. Z. Liu, A. Yu and J. Y. Lee, *Journal of Power Sources*, 1999, **81–82**, 416-419.
26. A. Bhaskar, S. Krueger, V. Siozios, J. Li, S. Nowak and M. Winter, *Advanced Energy Materials*, 2015, **5**, 1401156-1401157.
27. D. Luo, G. S. Li, C. C. Fu, J. Zheng, J. M. Fan, Q. Li and L. P. Li, *Advanced Energy Materials*, 2014, **4**, 1400062-1400071.
28. Q. Xia, X. Zhao, M. Xu, Z. Ding, J. Liu, L. Chen, D. G. Ivey and W. Wei, *J. Mater. Chem. A*, 2015, **3**, 3995-4003.
29. G. Singh, W. C. West, J. Soler and R. S. Katiyar, *Journal of Power Sources*, 2012, **218**, 34-38.

30. C. Venkateswara Rao, J. Soler, R. Katiyar, J. Shojan, W. C. West and R. S. Katiyar, *The Journal of Physical Chemistry C*, 2014, **118**, 14133-14141.
31. S. Hy, F. Felix, J. Rick, W. N. Su and B. J. Hwang, *Journal of the American Chemical Society*, 2013, **136**, 999-1007.
32. D. Kim, G. Sandi, J. R. Croy, K. G. Gallagher, S. H. Kang, E. Lee, M. D. Slater, C. S. Johnson and M. M. Thackeray, *J. Electrochem. Soc.*, 2013, **160**, A31-A38.
33. I. Bloom, L. Trahey, A. Abouimrane, I. Belharouak, X. Zhang, Q. Wu, W. Lu, D. P. Abraham, M. Bettge, J. W. Elam, X. Meng, A. K. Burrell, C. Ban, R. Tenent, J. Nanda and N. Dudney, *Journal of Power Sources*, 2014, **249**, 509-514.
34. J. Zheng, M. Gu, J. Xiao, B. J. Polzin, P. Yan, X. Chen, C. Wang and J.-G. Zhang, *Chemistry of Materials*, 2014, **26**, 6320-6327.